

# JGR Space Physics

## RESEARCH ARTICLE

10.1029/2019JA027167

### Key Points:

- Electron densities in Venus's ionosphere respond more strongly to solar activity changes with increasing altitude above the ionospheric peak
- Photochemical models are used to reproduce observed electron density profiles and assess causes of this behavior
- Large-scale inflation of the neutral atmosphere with increasing solar activity causes the enhanced response with increasing altitude

### Correspondence to:

K. Hensley,  
khens@bu.edu

### Citation:

Hensley, K., Withers, P., Girazian, Z., Pätzold, M., Tellmann, S., & Häusler, B. (2020). Dependence of dayside electron densities at Venus on solar irradiance. *Journal of Geophysical Research: Space Physics*, 125, e2019JA027167. <https://doi.org/10.1029/2019JA027167>

Received 17 JUL 2019

Accepted 11 JAN 2020

Accepted article online 3 FEB 2020

## Dependence of Dayside Electron Densities at Venus on Solar Irradiance

**K. Hensley<sup>1</sup> , P. Withers<sup>1,2</sup> , Z. Girazian<sup>3</sup> , M. Pätzold<sup>4</sup>, S. Tellmann<sup>4</sup>, and B. Häusler<sup>5</sup> **

<sup>1</sup>Department of Astronomy, Boston University, Boston, MA, USA, <sup>2</sup>Center for Space Physics, Boston University, Boston, MA, USA, <sup>3</sup>Department of Physics and Astronomy, University of Iowa, Iowa City, IA, USA, <sup>4</sup>Rheinisches Institut für Umweltforschung, Abteilung Planetenforschung, an der Universität zu Köln, Cologne, Germany, <sup>5</sup>Institut für Raumfahrttechnik und Weltraumnutzung, Universität der Bundeswehr München, Neubiberg, Germany

**Abstract** The ionosphere of Venus is a weakly ionized plasma layer embedded in the planet's upper atmosphere. Planetary ionospheres provide an excellent opportunity to study how our variable Sun affects the planets in our solar system. Because ionospheres are reservoirs from which atmospheric species can be lost to space, studying how ionospheres respond to changes in solar activity can help us understand how planetary atmospheres have evolved since their formation. While variations of the main and lower ionospheric peaks of Venus have been well studied, the behavior of the ionosphere above the altitude of the greatest electron density has not been fully constrained. To investigate the behavior of this region, we use electron density profiles obtained by the Venus Radio Science experiment aboard Venus Express. An increase in the response of the electron density to increasing solar irradiance with increasing altitude above the peak is readily apparent in these data. By using a one-dimensional photochemical equilibrium model to investigate the factors that drive the variations of the ionosphere of Venus, we find that changes in the composition of the underlying neutral atmosphere are responsible for the observed increase in ionospheric response with altitude.

### 1. Introduction

Incident solar extreme ultraviolet (EUV) and X-ray photons ionize atoms and molecules in a planet's atmosphere, generating a layer of weakly ionized plasma called an ionosphere. The characteristics of an ionosphere are largely determined by the planet's surface gravity, neutral atmospheric composition, orbital distance, rotation rate, and magnetic field (Schunk & Nagy, 2009). The spectrum of the incident ionizing radiation also has a significant impact on the vertical structure of a planetary ionosphere (e.g., Girazian et al., 2015).

The ionosphere of Venus has been studied extensively, starting with the radio occultation during the Mariner 5 flyby in 1967 (Kliore et al., 1967; Mariner Stanford Group, 1967). Subsequent missions, especially National Aeronautics and Space Administration's Pioneer Venus Orbiter (PVO) from 1978 to 1992 and European Space Agency's Venus Express (VEX) from 2006 to 2015, provided an in-depth look at the nature of Venus's thermosphere and ionosphere (e.g., Bauer et al., 1977; Brace & Kliore, 1991; Brace et al., 1979; Gérard et al., 2017; Häusler et al., 2006; Pätzold et al., 2007). Although CO<sub>2</sub> is by far the most abundant neutral species at altitudes up to ~160 km, the dominant ion from ~115 to ~180 km is O<sub>2</sub><sup>+</sup> (Brace & Kliore, 1991; Fox & Sung, 2001; Hedin et al., 1983). This results from the rapid interaction of CO<sub>2</sub><sup>+</sup> ions generated by photoionization and electron-impact ionization with small amounts (~5% at 140 km) of neutral atomic oxygen. The O<sub>2</sub><sup>+</sup> ions are lost through dissociative recombination (Fox, 2004). The main photochemical processes at work in the region of greatest plasma density are as follows (Schunk & Nagy, 2009):



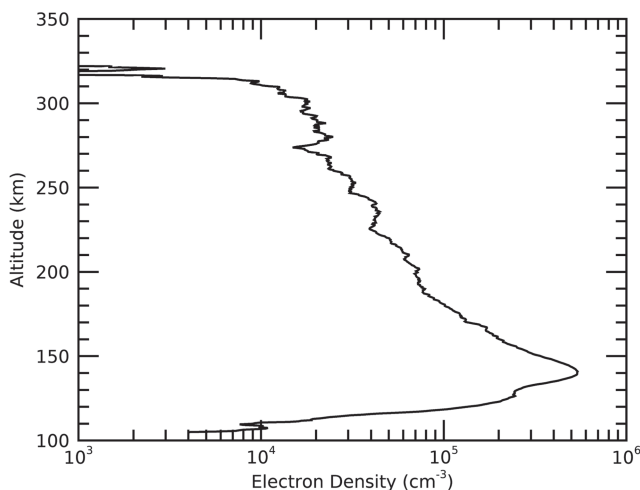


**Figure 1.** A typical Venus dayside electron density profile from Venus Express. This observation was made on 6 July 2012, at a solar zenith angle of 36°, latitude of 12.1°, and longitude of 284.3°. The  $F_{10.7P}$  value was 280 sfu at Venus. See section 2.2 for a discussion of the solar activity proxy,  $F_{10.7P}$ .

observations of the dayside ionosphere of Venus. The ionosphere of Venus exhibits clear maxima in the electron density at approximately 127 and 140 km. The upper (V2) peak is produced mainly by ionization due to solar EUV photons. The lower (V1) peak, on the other hand, is produced by ionization due to solar X-ray photons as well as electron-impact ionization. The dominant ion at both peaks is  $O_2^+$  (Fox & Sung, 2001). Below the V1 peak there exists a sporadic third layer (Pätzold et al., 2009).

A goal of planetary ionospheric studies is to understand how ionospheres change in response to changing solar activity, which manifests itself as cyclical fluctuations in solar X-ray, EUV, and radio emissions, as well as changes in the frequency of sunspots, solar flares, and coronal mass ejections. Central to this question is how solar activity affects the electron densities throughout the dayside ionosphere.

Simple photochemical equilibrium (PCE) theory describes how an idealized ionosphere behaves with changing altitude, solar zenith angle (SZA), and incident solar flux (Schunk & Nagy, 2009). Based on this theory, which employs a number of simplifying assumptions about the composition and thermal structure of the neutral atmosphere, as well as the incident solar flux, the dayside ionosphere of Venus should respond uniformly to solar activity variations at all altitudes (e.g., Fox & Kliore, 1997).

However, reality is more complex; Venus's dayside ionosphere can be sep-

arated into distinct regions, which may respond differently to changing solar irradiance. The ionosphere can be divided into two regions based on the dominant physical processes. Below  $\sim 180$  km is the PCE region, in which plasma is generated by photoionization and electron-impact ionization (Nagy et al., 1980). Above  $\sim 180$  km, transport processes dominate.

The effect of solar cycle variations on the V2 peak, the V1 peak, and the ionopause has been explored using in situ and remote sensing data by Kliore and Mullen (1989), Girazian et al. (2015), and Phillips et al. (1985), respectively, but the PCE region above the main ionospheric peak exhibits interesting behavior as well. Taylor et al. (1981) analyzed in situ measurements of  $O^+$ ,  $O_2^+$ ,  $C^+$ , and  $CO_2^+$  densities between the altitudes of 180 and 220 km and found that the densities of these ions were correlated with the Sun's flux at a wavelength of 10.7 cm, indicating that solar activity has a discernible impact on the conditions in the dayside ionosphere at these altitudes. Elphic et al. (1984) used in situ electron density measurements from the Orbiter Electron Temperature Probe aboard PVO to assess how the electron density in Venus's ionosphere responds to changing solar activity, for which they used the photoelectron current measured by the Langmuir probe as a proxy. After normalizing the observed electron densities to the empirical model of Theis et al. (1984) to remove the effects of changing SZA, they divided the measurements into two altitude bins (above and below 160 km) and fit a power law to the data in each bin in order to quantify the response of each altitude region to changing solar activity. The power law index was larger in the 160–200 km bin than in the  $\sim 150$ - to 160-km bin—0.89 and 0.33, respectively—leading them to conclude that electron densities at high altitudes increased more with increasing solar activity than those at low altitudes. In their review of the solar cycle variations of Venus's ionosphere, Fox and Kliore (1997) noted that in PVO radio occultation observations the electron density at the V2 peak increased by 50% from solar minimum to solar maximum but increased by a factor of 10 at 300 km, far above the PCE region (Kliore & Luhmann, 1991). More recently, Fox and Sung (2001) found that the electron density in their numerical models increased by 50–60% at the V2 peak and by a factor of four at 200 km from solar minimum to solar maximum.

The VEX radio occultation data set, described further in section 2.1, also clearly demonstrates an altitude dependence of the electron density response to changing solar activity, as shown in Figure 2. Figure 2 shows that the smallest response to increasing solar activity occurs near the V2 peak at  $\sim 140$  km. The relative increase in electron density is greater above and below the V2 peak than near the peak; at 140 km, the electron density increases  $\sim 40\%$ , while at 200 km it increases  $\sim 260\%$ . The cause of the marked increase in response with altitude between 140 and 180 km has not been fully explored.

The aim of this article is to determine how the electron densities in Venus's dayside ionosphere at altitudes between the V2 peak at 140 km and the top of the PCE region at  $\sim 180$  km respond to changes in solar activity.

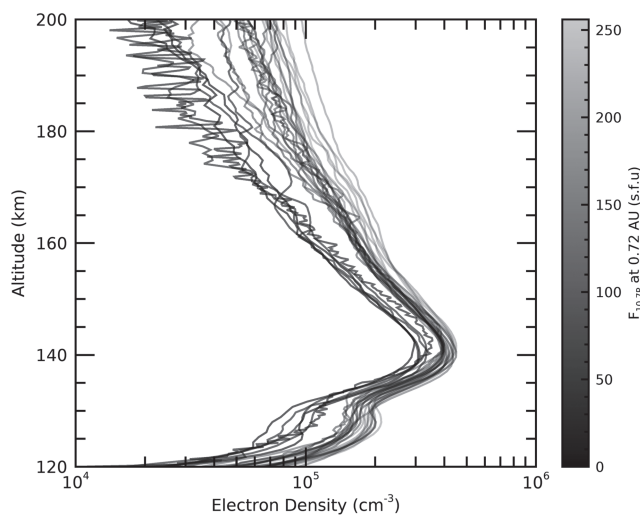


**Figure 2.** Venus Express electron density profiles with solar zenith angles between  $60^\circ$  and  $65^\circ$ . Dark gray profiles are from times of low solar activity, while light gray profiles are from times of high solar activity.  $F_{10.7P}$  has been converted to Venus's location (see section 2.2). For approximate values at Earth, divide by  $(1/0.723)^2 \approx 2$ .

the PVO data set, which is reported to contain 148 dayside profiles (Kliore & Luhmann, 1991). The VeRa data set encompasses the declining phase of Solar Cycle 23, the deep solar minimum that persisted throughout the first half of the mission, and the rise from solar minimum to solar maximum in 2014. The solar activity proxy, described in detail in the following subsection, increased by a factor of 3 over this time period. The set of dayside radio occultations spans SZAs from  $10^\circ$  to  $90^\circ$ . Examples of electron density profiles from this data set are shown in Figures 1 and 2.

## 2.2. Solar Activity Proxy

Ground-based measurements of the solar flux at a wavelength of 10.7 cm, referred to as  $F_{10.7}$ , are frequently used as a proxy for solar activity in ionospheric studies (e.g., Girazian, 2016; Kliore & Mullen, 1989). Other common proxies are  $F_{10.7A}$  (the running 81-day average  $F_{10.7}$  value) and  $F_{10.7P}$  (the average of  $F_{10.7}$  and  $F_{10.7A}$ ).

We elect to use  $F_{10.7P}$  as our solar activity proxy, which previous work (e.g., Mendillo et al., 2013) suggests is a better proxy for the Sun's ionizing irradiance than either  $F_{10.7}$  or  $F_{10.7A}$ .

We assigned  $F_{10.7P}$  values to each of the radio occultation profiles using measurements from the Dominion Radio Astrophysical Observatory, which reports a daily noontime  $F_{10.7}$  measurement corrected to 1 AU as well as monthly running averages (<https://ngdc.noaa.gov/stp/space-weather/solar-data/solar-features/solar-radio/noontime-flux/penticton/>).

Because Venus and Earth have different orbital distances and do not always face the same side of the Sun, the  $F_{10.7P}$  values must be adjusted to Venus's location. The adjustment employs values of the Venus-Sun distance and the Earth-Sun-Venus angle, which were obtained from the Jet Propulsion Laboratory HORIZONS database (<https://ssd.jpl.nasa.gov/horizons.cgi>). First, we used the Earth-Sun-Venus angle to calculate the number of days it would take for the Sun to rotate (forward or backward) so that the side facing Earth faces Venus. This date shift is used to select the appropriate  $F_{10.7P}$  value. Finally, the fluxes are converted from 1 AU to Venus's orbital distance by multiplying the  $F_{10.7P}$  values by  $\left(\frac{1\text{AU}}{d}\right)^2$ , where  $d$  is the Venus-Sun distance in AU. Figure 3 shows the

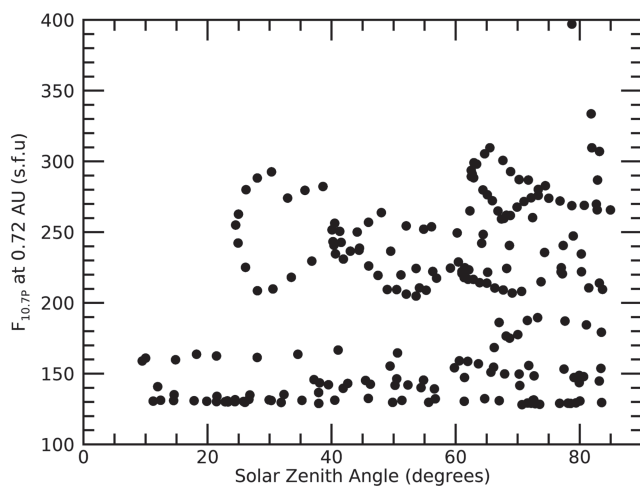


**Figure 3.** Solar zenith angle and solar activity coverage of the VeRa dayside radio occultation profiles. The  $F_{10.7P}$  values have been shifted to Venus's position. Profiles with SZA greater than  $85^\circ$  were not used in this study and are not shown here.

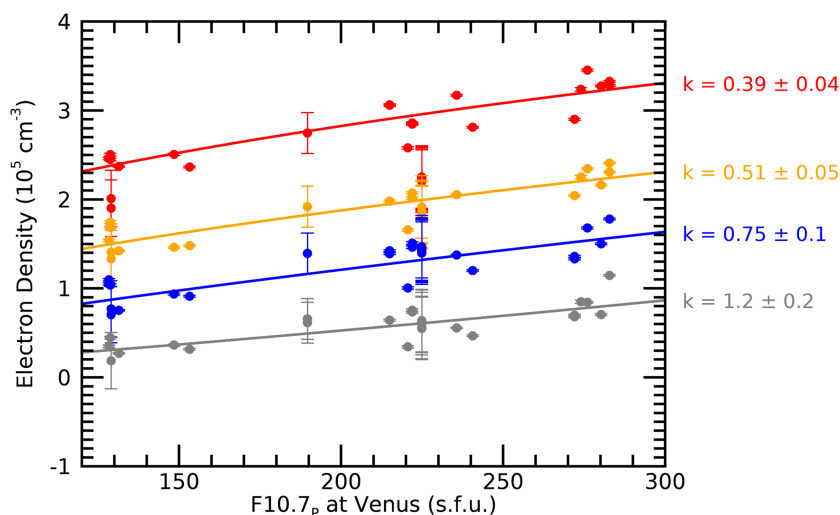


**Figure 4.** VEX electron density measurements with SZA =  $75 \pm 2.5^\circ$  for 140-, 150-, 160-, and 180-km altitudes (red, orange, blue, and gray, respectively). The 170-km measurements have been omitted for clarity. Altitude bins are 1 km high. The error bars indicate the 1-sigma error for each measurement.

$F_{10.7P}$  and SZA coverage of the 217 VeRa profiles used in this work. This data set has excellent SZA coverage, spanning nearly all dayside SZAs. At most dayside SZAs ( $\geq 30^\circ$ ), the  $F_{10.7P}$  values span a factor of 2 to 3.

### 3. Analysis of VEX Data

We first quantify the response of electron densities at altitudes between 125 and 180 km in Venus's dayside ionosphere to changing solar activity. To do this, we test a prediction of simple PCE theory, otherwise known as Chapman layer theory, that the electron density is proportional to the incident ionizing irradiance raised to an exponent  $k$  (Schunk & Nagy, 2009):

$$N_e = N_0 F_{10.7P}^k. \quad (4)$$

Simple PCE theory invokes several assumptions about a planet's neutral atmosphere and the incident ionizing flux. For example, the theory considers an atmosphere composed of a single neutral species, the ionization of which results in a single molecular ion species, which is then lost by dissociative recombination. The theory also assumes that the neutral atmosphere is uniform across all SZAs and that the density at a reference altitude is insensitive to changing SZA or solar activity. This theory does not consider additional neutral or ion species, solar activity-dependent changes in the neutral atmosphere, or changes to the electron temperature.

In the idealized case of this simple theory, the dayside ionosphere responds uniformly to changes in the incidence ionizing flux with the exponent in equation (4) equal to 0.5 at all altitudes (Fox & Kliore, 1997). While simple PCE theory predicts that  $k = 0.5$ , past studies of the main and lower peaks in the ionospheres of Venus and Mars (e.g., Fox & Yeager, 2009; Kliore & Mullen, 1989) indicate that this is not necessarily the case. Even at the main ionospheric peak, where the assumptions of PCE theory are largely satisfied, the value of  $k$  strongly depends on the choice of solar activity proxy (Girazian & Withers, 2013). Specifically, while  $F_{10.7P}$  rises and falls with the solar cycle in accordance with the Sun's ionizing flux, the relationship is not linear, resulting in a  $k$  value for the V2 peak that is less than the expected 0.5 (Kliore & Mullen, 1989). However, we are primarily concerned with the change in the value of  $k$  relative to the value at the V2 peak rather than the absolute value. Therefore, any proxy for the ionizing irradiance that has been shown to be useful for ionospheric studies (e.g.,  $F_{10.7}$  and  $F_{10.7P}$ ) will be suitable for our purposes.

Due to the ease of using  $F_{10.7P}$  compared to other solar activity proxies, we use  $F_{10.7P}$ , which is calculated from Earth-based  $F_{10.7}$  measurements, to determine the value of  $k$  for altitudes between 125 km and the top of the photochemically controlled region at  $\sim 180$  km (Kim et al., 1989). While several assumptions of simple PCE theory are increasingly violated at high altitudes, the exponent  $k$  is still a valuable metric for quantifying the response of the ionosphere to changes in solar activity.

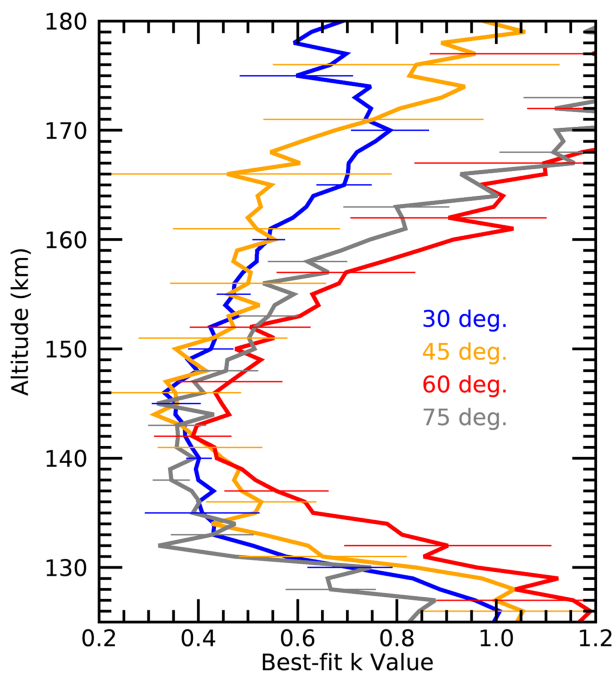


**Figure 5.** Best fit exponent  $k$  as a function of altitude for VEX profiles with SZA within  $2.5^\circ$  of  $30^\circ$ ,  $45^\circ$ ,  $60^\circ$ , and  $75^\circ$  SZA. Horizontal bars every 5 km represent the 1-sigma error.

activity proxies and corrected electron densities from all SZAs to the subsolar point rather than analyzing individual SZA bins. Using PVO radio occultations and a combination of  $F_{10.7}$  and EUV spectra from Atmosphere Explorer E, Kliore and Mullen (1989) found  $k = 0.376$ . More recently, Girazian (2016) combined VEX radio occultations with various observed and calculated solar activity proxies to derive  $k$  values between  $0.28 \pm 0.01$  and  $0.54 \pm 0.05$ . While not directly comparable, our result fits comfortably within the range of previous findings.

Figure 5 shows that the value of  $k$  changes little between approximately 135 and 150 km. This region represents the section of Venus's ionosphere where the assumptions of simple PCE theory, such as the presence of only one ion species, are largely satisfied. The sharp increase in  $k$  at altitudes below 130 km reflects the increased importance of electron-impact ionization below the main peak. The Sun's X-ray flux exhibits more variation from low to high solar activity than longer wavelengths (Girazian et al., 2015). Based on the  $F_{10.7P}$ -averaged model of the solar spectrum used in this work (see section 4.1 and figures therein), the solar photon flux increases by roughly 70% at 90 nm (the threshold wavelength for ionization of  $\text{CO}_2$ ) from  $F_{10.7P} = 65$  sfu to  $F_{10.7P} = 155$  sfu, while the flux at 10 nm increases by more than 300% over the same solar activity range. This effect is enhanced by an increase in electron-impact ionization, since an increase in the flux of photons with higher energies provides more energy to be imparted upon the resultant photoelectrons, which can cause further ionization through electron-impact ionization. Thus, the increasing value of  $k$  below 130 km reflects the fact that the source of ionization at those altitudes undergoes larger increases for a given increase in  $F_{10.7P}$  than altitudes near and above the peak.

Figure 5 shows that the value of  $k$  increases markedly above 150 km. At 180 km,  $k$  spans values from  $0.69 \pm 0.11$  to  $1.33 \pm 0.36$ . However, because the primary source of ionization at the main ionospheric peak and above is EUV irradiance rather than the more variable X-ray irradiance, we cannot use the large increase in X-ray irradiance and the associated electron-impact ionization to explain why the electron densities at altitudes between 150 and 180 km increase more with a given increase in solar activity than those near the peak. We specifically consider three factors that could control the behavior of the electron densities at these altitudes:

1. *Changes in the importance of minor ions.* Venus's ionosphere is made up of several ion species, the relative abundance of which is a function of altitude (see section 4.2 and figures therein). The presence of multiple ion species is not accounted for in simple PCE theory, which describes the characteristics of an ionosphere

Data scarcity near the subsolar point, as shown in Figure 3, limits our analysis to  $\text{SZA} \geq 30^\circ$ . At smaller SZA, the observations span only a 30% change in  $F_{10.7P}$ , whereas at higher SZA they span a factor of 3 variation. For  $5^\circ$  wide bins centered on  $30^\circ$ ,  $45^\circ$ ,  $60^\circ$ , and  $75^\circ$  SZA, we calculate the best fit exponent  $k$  at each altitude. We first linearize  $N_e = N_0 F_{10.7P}^k$  and rewrite it as  $\ln N_e = \ln N_0 + k \ln F_{10.7P}$ . We follow the fitting technique outlined in Girazian et al. (2015), in which the measurement uncertainty for each electron density profile, which is far smaller than the scatter in the data, provides the relative uncertainty for the least squares fitting. The overall magnitude of the error is then allowed to increase until the chi-square value equals one. Figure 4 shows the raw data and resultant best fit lines for four altitude bins at one SZA.

By fitting equation (4) to all the data in each 1-km altitude and  $5^\circ$  SZA bin, we obtain vertical profiles for the best fit  $k$  value for four SZA bins. Since we are interested in the behavior of the photochemically controlled region of the dayside ionosphere, we perform the fits at altitudes between 125 km and the top of the photochemically controlled region at 180 km. The best fit  $k$  values for all altitudes and SZAs considered in this work are provided in Appendix A.

Figure 5 shows the best fit  $k$  values as a function of altitude for the SZAs considered in this work. Near the main ionospheric peak at 140 km, the values of  $k$  range from  $0.39 \pm 0.04$  to  $0.45 \pm 0.12$ . This result is comparable to past studies of Venus's main ionospheric peak (Girazian, 2016; Kliore & Mullen, 1989), although those studies used different solar

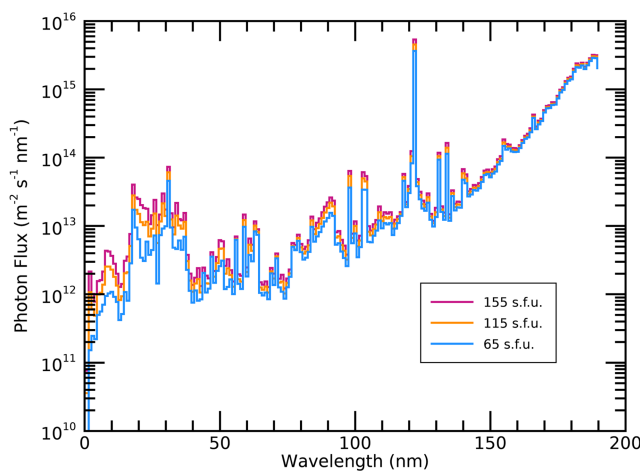


**Figure 6.** Model solar spectra for three levels of solar activity. Fluxes shown are for a distance of 1 AU. Increased variability at shorter wavelengths is apparent.

composed of one molecular ion species. A change in the ratio of minor to major ion species—which may be either atomic or molecular ion species with different dominant loss mechanisms which proceed at different rates—may affect the ionosphere's response to changing solar activity.

2. *Changes in the electron temperature.* The electron temperature directly impacts the electron density by determining the rate of dissociative recombination of molecular ions, including the dominant ion species,  $O_2^+$  (Schunk & Nagy, 2009). Higher electron temperatures decrease the dissociative recombination rate, which results in increased electron densities. Because of this, changes in the electron temperature with solar activity have the potential to strongly influence the response of the ionosphere to changing solar activity.
3. *Changes in the underlying neutral atmosphere.* The composition of Venus's neutral atmosphere is a function of altitude.  $CO_2$  is the dominant neutral below  $\sim 160$  km, at which point O takes over as the most abundant (Hedin et al., 1983). At a given altitude, the neutral composition is also a function of solar activity, as a result of the changing neutral temperature which causes the atmosphere to “puff up” at times of high solar activity. Because the ionosphere is embedded within the neutral atmosphere, this large-scale inflation of the neutral atmosphere has direct consequences for the ionosphere.

In order to investigate which of the above three factors determines how Venus's ionosphere responds to changing solar activity, we use a one-dimensional PCE model to calculate the ion and electron densities in Venus's ionosphere under a broad range of solar irradiances.

#### 4. Model Components and Output

This model was adapted from the Boston University Mars Ionosphere Model (Fallows et al., 2015) and translated to Venus by Girazian (2016). Here we briefly describe the components of the model and demonstrate the model's performance.

##### 4.1. Solar Spectrum

The ionizing irradiance is derived from EUV and X-ray solar spectra obtained by the Solar EUV Experiment (SEE) aboard the Thermosphere Ionosphere Mesosphere Energetics and Dynamics (TIMED) spacecraft. Nearly 3,000 solar EUV and X-ray spectra from TIMED-SEE were used to generate average solar spectra at 1 AU for  $F_{10.7P}$  values between 65 and 155 sfu in increments of 10 sfu. This process is described in greater detail in Girazian and Withers (2015). Model solar spectra for low, medium, and high solar activity are shown in Figure 6. Solar irradiance is converted to Venus's location by multiplying the fluxes by  $\left(\frac{1AU}{d}\right)^2$ , where  $d$  is the Venus-Sun distance in AU.

##### 4.2. Neutral Atmosphere

The underlying neutral atmosphere is the VTS3 model from Hedin et al. (1983). It is an empirical model based on in situ measurements of the neutral composition and temperature taken by the Orbiter Neutral Mass Spectrometer aboard PVO between 23 December 1978 and 16 August 1980. To reconcile the difference

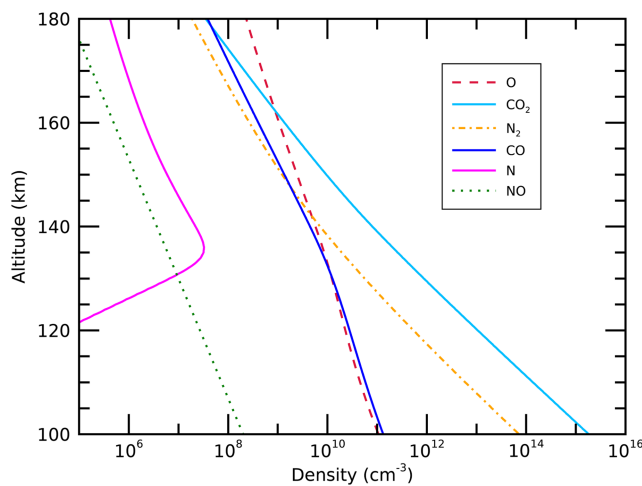


**Figure 7.** Sample model neutral atmosphere for SZA = 30° and  $F_{10.7P} = 65$  sfu.

in bulk atmospheric density between the PVO Orbiter Neutral Mass Spectrometer data and the Pioneer Venus entry probes, the VTS3 model includes a multiplicative correction factor of 1.63 for all neutral species. The VTS3 model gives neutral densities for six atmospheric species—CO<sub>2</sub>, O, N, CO, N<sub>2</sub>, and He—as well as the neutral temperature. These parameters are given as a function of altitude, latitude, local solar time, and solar activity. The VTS3 model represents long- and short-term variations in solar activity by utilizing both a 1-day value of  $F_{10.7}$  as well as the 81-day average value,  $F_{10.7A}$ , which are averaged to yield  $F_{10.7P}$ . In our implementation of the model, we assume that  $F_{10.7}$  and its 81-day average are equal, which allows us to use the  $F_{10.7P}$ -averaged solar spectra described in section 4.1.

We make several additional adjustments and improvements to the VTS3 model. First, we translate the model from the original FORTRAN to IDL. Second, following Girazian (2016), we include NO, the density of which is based on model calculations by Fox and Sung (2001). Third, we adjust the N densities, which in the VTS3 model are derived from calculations by Rusch and Cravens (1979), to be more consistent with model calculations by Fox and Sung (2001).

Finally, in agreement with previous modeling efforts (e.g., Cravens et al., 1981), we find that the use of the VTS3 neutral atmosphere in our ionospheric model leads to incorrect predictions of the V2 peak altitude. Similar to Cravens et al. (1981), we used a SZA-dependent neutral atmosphere correction to reproduce observed V2 peak altitudes. Here, we have scaled the VTS3 neutral atmosphere so that the peak altitude for each model electron density profile is equal to the average observed V2 peak altitude of 141 km (Girazian, 2016). The multiplicative factor varies with both SZA and solar activity. Figure 7 shows an example of vertical neutral density profiles used.

#### 4.3. Photochemistry

The photochemical scheme used by this model is laid out in Table 1. All reaction rates are taken from Schunk and Nagy (2009). Because there are no electron temperature measurements below 150 km, we adopt the

**Table 1**  
*List of Photochemical Reactions*

Reaction	Rate coefficient (cm <sup>3</sup> /s)
CO <sub>2</sub> <sup>+</sup> + O → O <sup>+</sup> + CO <sub>2</sub>	$k_1 = 9.6 \times 10^{-11}$
CO <sub>2</sub> <sup>+</sup> + O → O <sub>2</sub> <sup>+</sup> + CO	$k_2 = 1.6 \times 10^{-10}$
CO <sub>2</sub> <sup>+</sup> + NO → NO <sup>+</sup> + CO <sub>2</sub>	$k_3 = 1.2 \times 10^{-10}$
N <sub>2</sub> <sup>+</sup> + CO <sub>2</sub> → CO <sub>2</sub> <sup>+</sup> + N <sub>2</sub>	$k_4 = 8.0 \times 10^{-10}$
N <sub>2</sub> <sup>+</sup> + O → O <sup>+</sup> + N <sub>2</sub>	$k_5 = 9.8 \times 10^{-12}$
N <sub>2</sub> <sup>+</sup> + O → NO <sup>+</sup> + N	$k_6 = 1.3 \times 10^{-10}$
N <sub>2</sub> <sup>+</sup> + NO → NO <sup>+</sup> + N <sub>2</sub>	$k_7 = 4.1 \times 10^{-10}$
O <sup>+</sup> + NO → NO <sup>+</sup> + O	$k_8 = 8.0 \times 10^{-13}$
O <sup>+</sup> + N <sub>2</sub> → NO <sup>+</sup> + N	$k_9 = 1.2 \times 10^{-12}$
O <sup>+</sup> + CO <sub>2</sub> → O <sub>2</sub> <sup>+</sup> + CO	$k_{10} = 1.1 \times 10^{-9}$
O <sub>2</sub> <sup>+</sup> + NO → NO <sup>+</sup> + O <sub>2</sub>	$k_{11} = 4.6 \times 10^{-10}$
O <sub>2</sub> <sup>+</sup> + N → NO <sup>+</sup> + O	$k_{12} = 1.5 \times 10^{-10}$
O <sub>2</sub> <sup>+</sup> + e <sup>-</sup> → O + O	$\alpha_1 = 2.4 \times 10^{-7} \left(\frac{300 \text{ K}}{T_e}\right)^{0.70}$
CO <sub>2</sub> <sup>+</sup> + e <sup>-</sup> → CO + O	$\alpha_2 = 4.2 \times 10^{-7} \left(\frac{300 \text{ K}}{T_e}\right)^{0.75}$
N <sub>2</sub> <sup>+</sup> + e <sup>-</sup> → N + N	$\alpha_3 = 2.2 \times 10^{-7} \left(\frac{300 \text{ K}}{T_e}\right)^{0.39}$
NO <sup>+</sup> + e <sup>-</sup> → N + O	$\alpha_4 = 4.0 \times 10^{-7} \left(\frac{300 \text{ K}}{T_e}\right)^{0.50}$

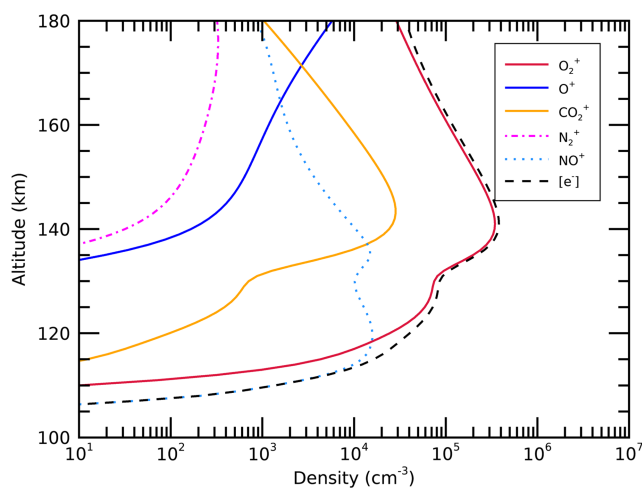


**Figure 8.** Model ion and electron densities for  $F_{10.7P} = 65$  sfu and SZA = 30°.

electron temperature model developed by Cravens et al. (1980), which has been used in previous Venus ionosphere models such as Fox and Sung (2001).

Absorption and ionization cross sections for all species were taken from the PHoto Ionization/Dissociation RATES (PHIDRATES; <http://phidrates.space.swri.edu>) database. Because the PHIDRATES cross sections do not have the same wavelength resolution as the TIMED-SEE spectra, the cross sections have been averaged to match the 1-nm bins of the solar spectra.

This model accounts for electron-impact ionization via the W-value method. This technique assumes that after a photon ionizes an atom or molecule, any energy that remains is used for electron-impact ionization. The “W-value”—the average amount of energy needed for each electron-impact ionization—depends upon the composition of the atmosphere and varies from planet to planet. For Venus, this value is 28.7 eV (Wedlund et al., 2011). Accurate parameterization of electron-impact ionization is especially important at low altitudes, where soft X-ray photons with energies greatly exceeding the ionization threshold of CO<sub>2</sub> are absorbed.

#### 4.4. Electron Density Profiles

We obtain model electron density profiles for SZA values of 0°, 15°, 30°, 45°, 60°, and 75°. For each SZA value, we run the model with  $F_{10.7P}$  equal to 65, 75, 85, 95, 105, 115, 125, 135, 145, and 155 sfu (values given at 1 AU; multiply by  $1/0.723^2 \approx 2$  for approximate values at Venus). The resulting set of 60 model electron density profiles encompass the dayside VEX radio occultation data set, with the exception of profiles near the limb.

At and above 180 km, transport processes become important and the assumption of PCE is no longer valid (Kim et al., 1989). Thus, the model profiles are usable between the base of the neutral atmosphere model at 100 km and the limit of PCE at ~180 km. Figure 8 shows the model output for low solar activity.

Figure 9 compares a subset of the VEX data to the corresponding model profiles. It shows all VEX profiles within 2.5° of 15°, 45°, and 75° SZA. Model profiles at these SZAs are shown only if their  $F_{10.7P}$  value is within the range spanned by the set of corresponding VEX profiles. For example, there are no observations with  $F_{10.7P} > 95$  sfu with SZA = 15 ± 2.5°, so the model profiles with  $F_{10.7P} \geq 95$  sfu are not shown. Qualitatively, the agreement between observations and model output appears good between 135 and 180 km. To assess the agreement quantitatively, we consider the average of all observed profiles in a panel and the average of

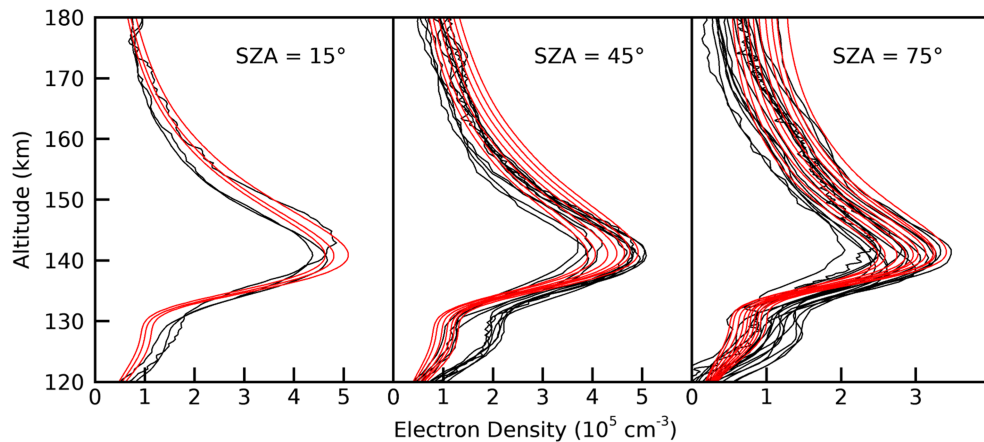


**Figure 9.** Data-model comparison for three SZA values. Model profiles (red) for a given SZA value are compared to VEX profiles (black) with SZA values within 2.5° of the model value. Since the observations near 15° are from a period of low solar activity, the high solar activity model profiles are not shown in the first panel. Note the change in the horizontal axis in the rightmost panel.

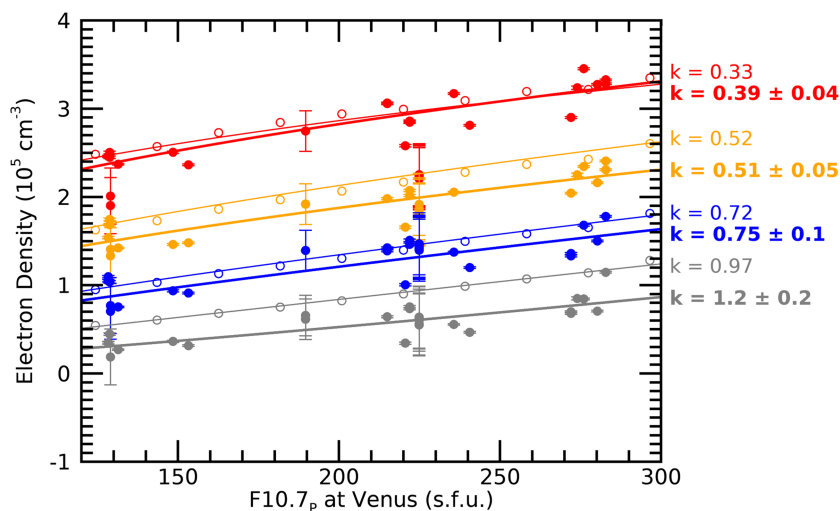


**Figure 10.** Comparison of VEX electron density measurements (filled circles) to model electron densities (open circles) with SZA =  $75 \pm 2.5^\circ$  for 140, 150, 160, and 180 km (red, orange, blue, and gray, respectively). The 170-km measurements and models are omitted for clarity. Altitude bins are 1 km high. The error bars indicate the 1-sigma error for each VEX measurement. Best fit  $k$  values are noted on the right, for both data (bold text) and models (regular text).

all model profile in that panel. The average model profiles are within 20% of the average data profiles for all altitudes between 135 and 180 km, with the exception of the SZA =  $75^\circ$  case, for which the model-data difference exceeds 20% from 170 to 180 km. This performance compares favorably to other models of Venus's ionosphere that have been compared to data, such as Ambili et al. (2019), Peter et al. (2014), Kim et al. (1989), Cravens et al. (1981), and Nagy et al. (1980).

In order to compare how the observed and modeled electron densities change in response to changing solar activity, we repeat the analysis outlined in section 3 and determine the best fit value of  $k$  as a function of altitude for the model profiles. Figure 10 shows raw data and model values for four altitude bins at one SZA, while Figure 11 compares  $k$  versus  $z$  profiles for four SZA values. The model broadly reproduces the observed  $k$  versus  $z$  behavior;  $k$  reaches a minimum near the V2 peak and increases steadily above the peak. The values of  $k$  that are derived from models show little dependence on SZA, while the values of  $k$  that are derived from observations show appreciable scatter, particularly at 160–180 km. Given the error bars, however, the observationally derived values of  $k$  could be consistent with no dependence of  $k$  on SZA. These results demonstrate that physics-based models of the ionosphere of Venus adequately reproduce the observed behavior of how ionospheric electron densities at 135–180 km depend on solar activity and altitude. In the remaining sections of this manuscript, we investigate the underlying reasons why these trends exist in observations and models.

## 5. Model Simplification

The above sections have demonstrated that the full PCE model adequately reproduces the observed changes in ionospheric electron density with solar activity and altitude. We turn now to deconstructing the full PCE model in order to develop understanding of why these trends occur. We pared the full PCE model down to its most important components to develop a simple, analytic expression for how the electron density varies as a function of atmospheric parameters. Developing a simple, analytic model is important because it allows us to isolate the components that have the most influence on the resultant electron density and manipulate them directly. This simplified model will allow us to directly investigate the impact of minor species, changing electron temperatures, and changing neutral atmosphere.

We accomplished this by eliminating all but the most important chemical reactions in Table 1. We first calculated the production and loss rates using the Hedin et al. (1983) neutral densities, reaction rate coefficients from Table 1, and our modeled ion and electron densities as inputs. Starting with  $O^+$ ,  $O_2^+$ , and  $CO_2^+$ , we calculated the reaction rate at 150, 160, 170, and 180 km for each of the reactions listed in Table 1. If a production or loss rate for a given reaction was substantially slower than the other production or loss rates for

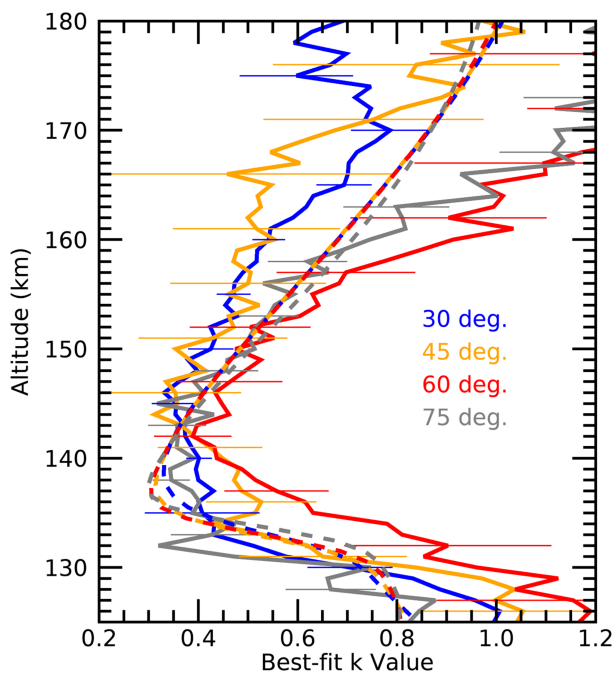


**Figure 11.** Comparison of best fit  $k$  values for data (solid lines) and models (dashed lines). The  $SZA = 0^\circ$  model result has been omitted since there are no data at that  $SZA$  to compare to. The  $SZA = 15^\circ$  model and data results have been omitted since there is insufficient  $F_{10.7P}$  coverage at that  $SZA$ . Horizontal bars every 5 km represent the 1-sigma error. Note that there is significant overlap between the  $30^\circ$ ,  $45^\circ$ , and  $60^\circ$  model curves between 140 and 170 km.

that species, it was eliminated. In almost all cases, the production and loss rates for reactions involving N, NO, and  $N_2$  or their ions were at least an order of magnitude slower than those without. As a result, all reactions involving N, NO, and  $N_2$  were eliminated, reducing the 16 equations in Table 1 to just 5. In addition to the photoionization of  $CO_2$  and O, the relevant reactions are as follows:



Assuming PCE (i.e., the ion production rate is equal to the loss rate for each ion species and the sum of the ion densities is equal to the electron density) and solving the resultant system of equations yields a cubic expression for the electron density that depends on the neutral atomic oxygen and carbon dioxide densities, the  $O_2^+$  and  $CO_2^+$  recombination rate coefficients, and the ion-neutral rate coefficients. Further details of this calculation are provided in Appendix B. Retaining the  $[e^-]^2$  and  $[e^-]^0$  terms in equation (B4), the absolute magnitudes of which are typically 1 to 2 orders of magnitude larger than the remaining two terms, yields a simple analytic expression for the electron density:

$$n_e \approx \sqrt{\frac{P_{O^+} + P_{CO_2^+}}{\alpha_1}} \quad (10)$$

Here,  $P_{O^+}$  and  $P_{CO_2^+}$  are the production rates for  $O^+$  and  $CO_2^+$ , respectively. These quantities are given by the combined photoproduction and electron-impact production rates. The photoionization rates are given by  $n_O \sum \sigma_O(\lambda)F(\lambda)$  and  $n_{CO_2} \sum \sigma_{CO_2}(\lambda)F(\lambda)$ , in which the sums are calculated from  $\lambda = 0.5$  nm to the longest wavelength capable of ionizing the neutral species. Electron-impact ionization is accounted for by adding a multiplicative factor to the photo-production rate. The electron-impact ionization rate is nearly constant at altitudes where little attenuation of the solar flux occurs ( $>150$  km), so while the inclusion of electron-impact ionization affects the calculated electron densities, it does not affect the resultant value of  $k$ .  $\alpha_1$  is the dissociative recombination rate coefficient of  $O_2^+$ . This expression approximates the ionosphere as one in which neutral O and  $CO_2$  are photoionized to yield  $O^+$  and  $CO_2^+$ , which are then entirely and instantaneously converted to  $O_2^+$  by ion-neutral reactions. The  $O_2^+$  ions are then lost by dissociative recombination.

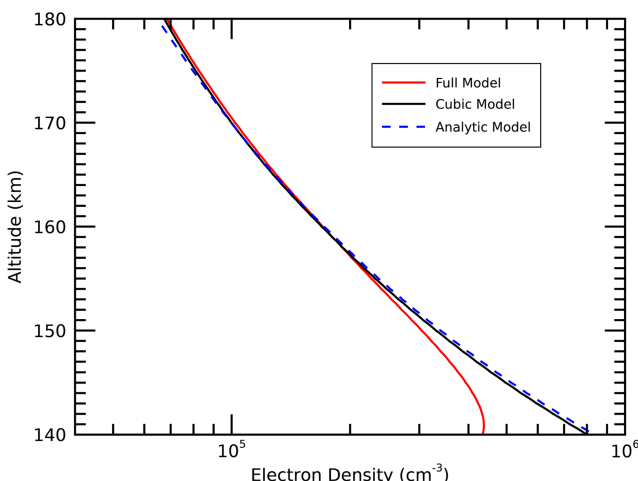


**Figure 12.** A comparison of electron densities from the full 1-D PCE model, the simplified cubic model, and the simplified analytic model. Profiles are shown for  $F_{10.7P} = 65$  sfu and  $SZA = 30^\circ$ .

For simplicity, our model formulation does not include attenuation of the solar flux by absorption, as most altitudes of interest are in the optically thin regime where absorption is negligible. Figure 12 shows an example of the output of the full PCE model compared to our simplified model. The electron densities calculated using the analytic model are within 15% of the full PCE model densities at all altitudes between 155 and 180 km. Above 170 km, the analytic model electron densities tend to be slightly smaller than the full model electron densities. This is a result of the simplified photochemical scheme, in which the long-lived atomic oxygen

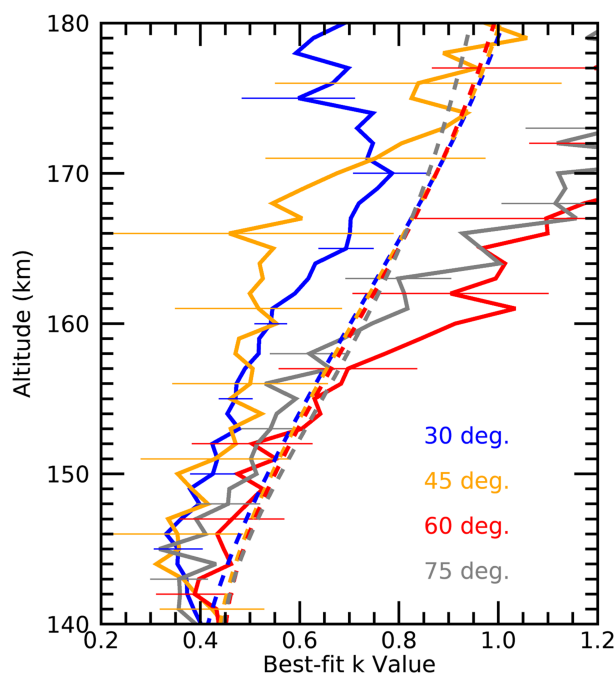


**Figure 13.** Comparison of best fit  $k$  values for data (solid lines) and simplified analytic models (dashed lines). Horizontal bars every 5 km represent the 1-sigma error. Note that there is significant overlap between models.

ions are essentially converted into molecular oxygen ions, which are quickly lost through dissociative recombination. The discrepancy at lower altitudes is due to the lack of attenuation of the solar irradiance in the analytic model.

Figure 13 compares the best fit exponent  $k$  as a function of altitude for the VEX data and the simplified analytic model. Comparison of Figure 11 and Figure 13 shows that high-altitude values of  $k$  are the same for the full PCE model and the simplified analytic model, as suggested by Figure 12. Even though modeled electron densities at low altitudes differ between the full PCE model and the simplified analytic model due to the simplifying omission of attenuation (Figure 12), the corresponding values of  $k$  are reasonably similar. Moreover, Figure 13 shows that values of  $k$  found from observations and from the simplified analytic model are in reasonable agreement. This demonstrates that the simplified analytic model is an appropriate tool to use to investigate why the observations (and the full PCE model) respond to changes in solar activity in the manner discussed in the previous sections.

Using this simplified analytic model, we can assess the impact that minor ions, electron temperature changes, and neutral atmosphere changes have on the behavior of Venus's ionosphere with changing solar activity.

## 6. Interpretation of Simplified Model Output

In this section we address the three hypotheses for the increase in  $k$  with altitude that are laid out in section 3.

### 6.1. Importance of Minor Ions

In addition to the major ions ( $O^+$ ,  $O_2^+$ , and  $CO_2^+$ ), Venus's ionosphere contains small amounts of  $N_2^+$  and  $NO^+$ , as shown in Figure 8. At 150 km, these two species make up approximately 2% of the total ion concentration. At the upper limit of our PCE model, 180 km, the contribution from the minor ion species increases to approximately 4%. This small proportion of minor ions does have the potential to change the behavior of the ionosphere, as outlined in section 3. However, our simplified analytic model includes only the three major ions does an excellent job of reproducing the behavior of the full model without the inclusion of these minor species. On these grounds we exclude the contribution of minor ions as a main contributor to the increase in the response of electron densities in Venus's ionosphere with altitude above the main peak.

### 6.2. Changes in the Electron Temperature

The question of how electron temperatures in Venus's ionosphere vary with solar activity has been investigated by Elphic et al. (1984), Kliore and Mullen (1989), and Brace and Theis (1996). Elphic et al. (1984) used in situ observations from PVO during solar maximum and an empirical model of electron temperatures and densities in Venus's ionosphere by Theis et al. (1984) to show that while the electron densities between 150 and 200 km vary considerably with changing solar activity, electron temperatures in the same altitude range remain roughly constant. Kliore and Mullen (1989) used the Venus International Reference Atmosphere and theoretical predictions for the production of  $CO_2^+$  to explore the response of the electron temperature to changing solar activity. Using this method, which employs a number of assumptions about conditions in the atmosphere near the ionospheric peak, they found that the electron temperature did increase with increasing solar activity—by 25% at the main peak and by 50–75% at altitudes above 200 km. In response to this finding, Brace and Theis (1996) expanded their analysis to include solar minimum preentry measurements by PVO. Using these in situ measurements, they found that the solar minimum electron temperatures in the ionosphere were essentially the same as those given in the Theis et al. (1984) empirical model, which draws from solar maximum measurements, refuting the findings of Kliore and Mullen (1989). Brace and Theis (1996) noted that this behavior is similar to Earth's ionosphere, in which increased electron densities at solar maximum result in higher electron collision and cooling rates, as found in Brace and Theis (1984).

Previous Venus ionosphere models (e.g., Fox & Sung, 2001) have used electron temperature profiles that vary with altitude but not solar activity. Similarly, we find no need to vary the electron temperature with solar

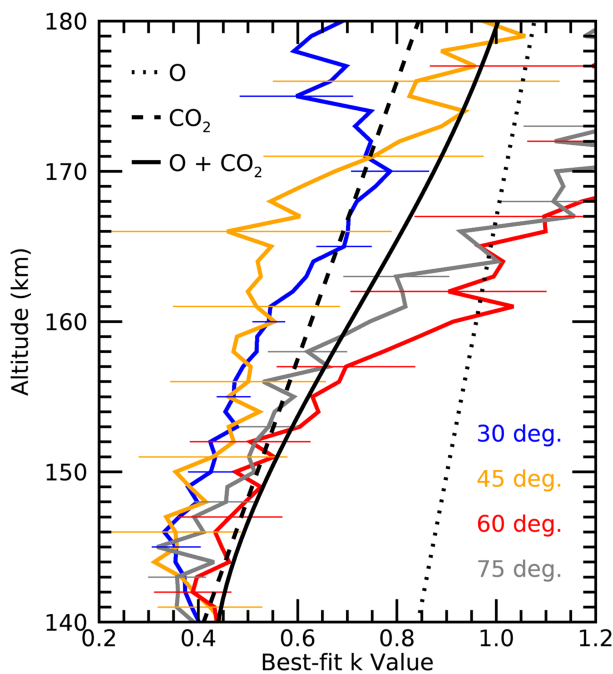


**Figure 14.** Comparison of  $k$  values as a function of altitude for the VEX observations (blue, orange, gray, and red solid lines), simplified analytic model (solid black line), and end-member models (dotted and dashed black lines). For clarity, only models with  $SZA = 45^\circ$  are shown.

reactions but are otherwise negligible. This  $\text{CO}_2$  end-member is directly applicable at low altitudes. In the second end-member, conditions in the neutral atmosphere are reversed such that the neutral atmosphere is composed only of O and trace amounts of  $\text{CO}_2$ . Production of ions by photoionization and electron-impact ionization produces only  $\text{O}^+$  ions. Trace amounts of neutral atomic oxygen are sufficient to permit the rapid conversion of  $\text{CO}_2^+$  ions into  $\text{O}_2^+$  ions by charge exchange reactions, but are otherwise negligible. This O end-member is directly applicable at high altitudes.

The electron densities for these two end-member cases are given by the following:

$$n_e \approx \sqrt{\frac{P_{\text{CO}_2^+}}{\alpha_1}} \quad (11)$$

$$n_e \approx \sqrt{\frac{P_{\text{O}^+}}{\alpha_1}} \quad (12)$$

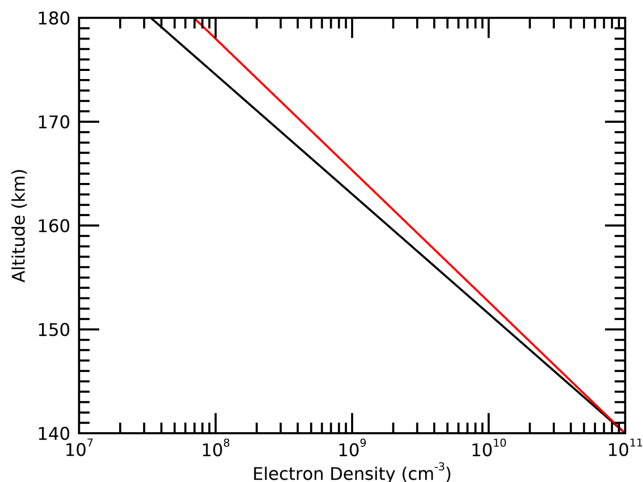


**Figure 15.** Demonstration of how the neutral  $\text{CO}_2$  density changes as the neutral atmosphere heats up. The lines shown here represent an idealized atmosphere in which the  $\text{CO}_2$  density falls off purely exponentially with altitude. From the black line to the red line there is a 10% increase in the neutral temperature.

activity to reproduce the observed changes in the electron density with increasing solar activity. In order to reproduce the observed increase in response with increasing altitude above the peak, not only would the electron temperatures need to increase with solar activity at all altitudes, the increase in electron temperature would also need to be larger at high altitudes. This is not supported by analysis of the available in situ data (e.g., Brace & Theis, 1996).

### 6.3. Changes in the Neutral Atmosphere

The compositions of the neutral atmosphere and ionosphere of Venus are related, as illustrated in Figures 7 and 8. At 140 km, the dominant neutral is  $\text{CO}_2$  (>80%) and the dominant ion is  $\text{O}_2^+$  (>90%) (Hedin et al., 1983; Knudsen et al., 1979; Niemann et al., 1979, 1980; Taylor et al., 1979, 1980). As outlined in section 1, this ionospheric composition arises from the rapid charge-exchange reaction of photo-produced  $\text{CO}_2^+$  ions with small amounts of neutral atomic oxygen (<5%), which forms  $\text{O}_2^+$  ions. At 180 km, the dominant neutral is atomic oxygen (>65%) and the  $\text{CO}_2$  abundance is on the order of 10%. Yet the dominant ion remains  $\text{O}_2^+$ . Here this ionospheric composition arises from the rapid charge-exchange reaction of photo-produced  $\text{O}^+$  ions with small amounts of neutral oxygen-bearing molecules (CO and  $\text{CO}_2$ ), which forms  $\text{O}_2^+$  ions.

These points suggest that two end-member cases of the simplified analytic model could be illuminating. In the first end-member, the neutral atmosphere is composed only of  $\text{CO}_2$  and trace amounts of O. Production of ions by photoionization and electron-impact ionization produces only  $\text{CO}_2^+$  ions. Trace amounts of neutral atomic oxygen are sufficient to permit the rapid conversion of  $\text{CO}_2^+$  ions into  $\text{O}_2^+$  ions by charge exchange

reactions but are otherwise negligible. This  $\text{CO}_2$  end-member is directly applicable at low altitudes. In the second end-member, conditions in the neutral atmosphere are reversed such that the neutral atmosphere is composed only of O and trace amounts of  $\text{CO}_2$ . Production of ions by photoionization and electron-impact ionization produces only  $\text{O}^+$  ions. Trace amounts of neutral carbon dioxide are sufficient to permit the rapid conversion of  $\text{O}^+$  ions into  $\text{O}_2^+$  ions by charge exchange reactions, but are otherwise negligible. This O end-member is directly applicable at high altitudes.

The electron densities for these two end-member cases are given by the following:

$$n_e \approx \sqrt{\frac{P_{\text{CO}_2^+}}{\alpha_1}} \quad (11)$$

$$n_e \approx \sqrt{\frac{P_{\text{O}^+}}{\alpha_1}} \quad (12)$$

These two end-members represent the low- and high-altitude thermosphere of Venus, respectively. Production rates in these equations were calculated using the same inputs as the full PCE model, as described in section 4. Figure 14 shows the behavior of the single-component atmospheres compared to the full atmosphere model and the data. It shows that, for each of the single-component atmospheres, the value of  $k$  increases steadily with increasing altitude. This behavior has a natural explanation. As solar activity increases, the neutral temperature in the thermosphere increases as well (Keating & Bouger, 1987). This causes an increase in the neutral scale height, which results in increased neutral densities at higher altitudes. An example for  $\text{CO}_2$  is shown in Figure 15. As the neutral temperature increases (by 10%, in this case), the  $\text{CO}_2$  density increases as well, and the highest percentage increase occurs at high altitudes.

Because ion production rates in the optically thin regime are directly proportional to neutral density, the increase in the neutral scale height also causes the greatest percentage increase in electron density at high altitudes, which leads to an increase in the value of  $k$ , even for an atmosphere that is dominated by a single neutral species.

Returning to Figure 14, the behavior of  $k$  for the simplified analytic model, which was found in Figure 13 to adequately represent observations, is intermediate between the behavior of the two end-member cases. Furthermore, the behavior of the simplified analytic model is close to the behavior of the CO<sub>2</sub> end-member case at low altitudes where CO<sub>2</sub> is the dominant neutral species but close to the behavior of the O end-member case at high altitudes where O is the dominant neutral species.

Thus, the changes observed in Venus's atmosphere are reflective of a neutral composition that changes with both altitude and solar activity. Specifically, the behavior of Venus's ionosphere at and below the altitude of maximum electron density, where atomic oxygen makes up less than 5% of the neutral atmosphere, closely mimics the behavior of an atmosphere dominated by CO<sub>2</sub>. As atomic oxygen becomes increasingly abundant at altitudes above the main ionospheric peak, the response of the ionosphere at those altitudes shifts to approach the behavior of an atmosphere dominated by atomic oxygen.

## 7. Conclusions

Electron densities at altitudes above Venus's main ionospheric peak vary dramatically with changes in solar activity. Previous studies such as Elphic et al. (1984) and Fox and Sung (2001) noted that the electron densities in this region reacted more strongly to changes in solar activity at higher altitudes than lower altitudes. Using 217 day-side radio occultation profiles from VEX, we confirm the qualitative findings of previous work. We also quantified the level of response of electron densities in Venus's ionosphere to changes in solar activity. To do this, we tested a prediction of PCE theory, previously confirmed at the V2 and V1 peaks, that electron densities follow the relation  $N_e \propto F^k$ . We calculated the best fit value of  $k$  in 1-km bins from 125 to 180 km and found that the value of  $k$  increases from the V2 peak at 140 km to the top of the PCE region at 180 km (e.g., from  $0.40 \pm 0.02$  to  $0.69 \pm 0.11$  for profiles with SZA =  $30 \pm 2.5^\circ$ ).

We found that a one-dimensional PCE model was able to adequately reproduce these observed trends in the response of ionospheric electron density to changes in solar activity. In order to investigate the underlying causes of this marked increase, we deconstructed this model to assess the impact of changes in the electron temperature, importance of minor ion species, and the neutral atmosphere. We found that changes in the neutral atmosphere are responsible for the observed increase in response of the electron densities with increasing altitude. Specifically, the observed increase in electron density response to changing solar activity with increasing altitude above the peak can be linked to changes to the neutral scale height and resultant changes to the neutral composition. We use end-member representations of Venus's ionosphere generated by photoionization of only a single neutral species to illustrate this point. With only carbon dioxide or atomic oxygen present—the limiting cases of the low- and high-altitude ionosphere of Venus, respectively—the calculated value of  $k$  still increases with altitude. This is due to the fact that increased solar EUV radiation increases the neutral temperature, which in turn increases the neutral scale height. An increase in the scale height for a given neutral species causes its density to increase, with the largest increases seen at higher altitudes. Because the ionosphere is embedded in the neutral atmosphere, this large-scale “puffing up” of the neutral atmosphere has direct consequences for the ionosphere. This fact alone is enough to explain the increase in the value of  $k$  above the altitude of peak density in Venus's ionosphere but does not explain the particular shape of the  $k$ -curve. The shape of the curve reflects the changing composition of the neutral atmosphere, which transitions from being dominated by carbon dioxide at low altitudes to atomic oxygen at high altitudes.

## Appendix A: Model Fits

Table A1 reports best fit  $k$  values for VEX data at 1-km resolution and SZAs of  $30^\circ$ ,  $45^\circ$ ,  $60^\circ$ , and  $75^\circ$ .

## Appendix B: Model Equations

We simplify the full PCE model of section 5 by retaining only the five most important ion-neutral reactions. Assuming PCE (i.e., the ion production rate is equal to the loss rate for each ion species and the sum of the

**Table A1**  
*Best Fit k Values for VEX Data*

Altitude (km)	Solar zenith angle (degrees)			
	30	45	60	75
125	0.99 ± 0.08	1.04 ± 0.22	1.17 ± 0.26	0.82 ± 0.11
126	1.01 ± 0.07	1.05 ± 0.21	1.19 ± 0.25	0.84 ± 0.09
127	0.96 ± 0.06	1.00 ± 0.19	1.15 ± 0.27	0.88 ± 0.10
128	0.89 ± 0.06	1.04 ± 0.20	1.04 ± 0.21	0.67 ± 0.09
129	0.83 ± 0.07	0.97 ± 0.16	1.12 ± 0.22	0.66 ± 0.08
130	0.71 ± 0.08	0.84 ± 0.15	0.96 ± 0.20	0.75 ± 0.07
131	0.58 ± 0.09	0.65 ± 0.17	0.85 ± 0.21	0.47 ± 0.08
132	0.51 ± 0.09	0.62 ± 0.20	0.90 ± 0.21	0.32 ± 0.08
133	0.43 ± 0.11	0.53 ± 0.22	0.81 ± 0.19	0.43 ± 0.08
134	0.43 ± 0.11	0.43 ± 0.20	0.78 ± 0.15	0.47 ± 0.08
135	0.41 ± 0.11	0.51 ± 0.16	0.63 ± 0.15	0.39 ± 0.08
136	0.40 ± 0.08	0.53 ± 0.11	0.61 ± 0.13	0.40 ± 0.06
137	0.43 ± 0.08	0.49 ± 0.11	0.56 ± 0.10	0.39 ± 0.05
138	0.40 ± 0.05	0.47 ± 0.10	0.52 ± 0.11	0.35 ± 0.04
139	0.39 ± 0.05	0.48 ± 0.11	0.49 ± 0.10	0.34 ± 0.04
140	0.40 ± 0.02	0.45 ± 0.12	0.44 ± 0.08	0.39 ± 0.04
141	0.39 ± 0.02	0.42 ± 0.10	0.43 ± 0.09	0.36 ± 0.05
142	0.37 ± 0.02	0.39 ± 0.12	0.39 ± 0.08	0.36 ± 0.05
143	0.37 ± 0.03	0.37 ± 0.12	0.40 ± 0.08	0.36 ± 0.06
144	0.35 ± 0.04	0.31 ± 0.13	0.46 ± 0.08	0.43 ± 0.06
145	0.36 ± 0.05	0.36 ± 0.11	0.45 ± 0.11	0.32 ± 0.06
146	0.33 ± 0.06	0.35 ± 0.13	0.43 ± 0.09	0.41 ± 0.06
147	0.36 ± 0.06	0.34 ± 0.15	0.46 ± 0.10	0.39 ± 0.06
148	0.40 ± 0.05	0.42 ± 0.14	0.49 ± 0.11	0.46 ± 0.06
149	0.38 ± 0.05	0.38 ± 0.12	0.53 ± 0.12	0.46 ± 0.06
150	0.43 ± 0.04	0.35 ± 0.13	0.47 ± 0.16	0.51 ± 0.05
151	0.43 ± 0.05	0.43 ± 0.15	0.55 ± 0.12	0.50 ± 0.05
152	0.42 ± 0.05	0.47 ± 0.13	0.50 ± 0.12	0.51 ± 0.06
153	0.48 ± 0.04	0.46 ± 0.16	0.60 ± 0.13	0.54 ± 0.06
154	0.45 ± 0.04	0.52 ± 0.18	0.64 ± 0.13	0.55 ± 0.07
155	0.47 ± 0.03	0.46 ± 0.21	0.63 ± 0.14	0.59 ± 0.07
156	0.47 ± 0.05	0.50 ± 0.16	0.68 ± 0.19	0.53 ± 0.07
157	0.49 ± 0.03	0.51 ± 0.16	0.70 ± 0.14	0.66 ± 0.08
158	0.52 ± 0.03	0.47 ± 0.16	0.77 ± 0.14	0.62 ± 0.08
159	0.52 ± 0.03	0.48 ± 0.15	0.84 ± 0.14	0.69 ± 0.08
160	0.54 ± 0.03	0.55 ± 0.15	0.91 ± 0.17	0.75 ± 0.10
161	0.55 ± 0.03	0.52 ± 0.17	1.03 ± 0.17	0.82 ± 0.10
162	0.59 ± 0.04	0.50 ± 0.19	0.90 ± 0.20	0.81 ± 0.11
163	0.62 ± 0.04	0.53 ± 0.17	0.99 ± 0.20	0.80 ± 0.11
164	0.63 ± 0.06	0.52 ± 0.23	1.01 ± 0.18	1.00 ± 0.11
165	0.69 ± 0.05	0.55 ± 0.31	0.97 ± 0.18	0.97 ± 0.12
166	0.70 ± 0.06	0.46 ± 0.33	1.10 ± 0.18	0.93 ± 0.11
167	0.70 ± 0.07	0.60 ± 0.30	1.10 ± 0.26	1.16 ± 0.14
168	0.72 ± 0.08	0.55 ± 0.36	1.17 ± 0.20	1.12 ± 0.11
169	0.76 ± 0.09	0.61 ± 0.37	1.29 ± 0.26	1.14 ± 0.16
170	0.79 ± 0.08	0.67 ± 0.41	1.34 ± 0.27	1.12 ± 0.14

**Table A1** *Continued*

Altitude (km)	Solar zenith angle (degrees)			
	30	45	60	75
171	0.74 ± 0.10	0.75 ± 0.22	1.36 ± 0.26	1.43 ± 0.18
172	0.75 ± 0.08	0.81 ± 0.27	1.34 ± 0.28	1.12 ± 0.15
173	0.72 ± 0.09	0.89 ± 0.43	1.30 ± 0.36	1.24 ± 0.18
174	0.75 ± 0.09	0.94 ± 0.53	1.36 ± 0.28	1.21 ± 0.17
175	0.60 ± 0.11	0.83 ± 0.37	1.30 ± 0.30	1.29 ± 0.21
176	0.67 ± 0.11	0.84 ± 0.29	1.53 ± 0.34	1.34 ± 0.21
177	0.70 ± 0.11	0.96 ± 0.17	1.19 ± 0.33	1.36 ± 0.19
178	0.59 ± 0.15	0.89 ± 0.18	1.27 ± 0.44	1.48 ± 0.20
179	0.63 ± 0.14	1.06 ± 0.31	1.41 ± 0.36	1.18 ± 0.22
180	0.69 ± 0.11	0.97 ± 0.51	1.33 ± 0.36	1.23 ± 0.22

ion densities is equal to the electron density) and solving the resultant system of equations yields a cubic expression for the electron density that depends on the neutral atomic oxygen and carbon dioxide densities, the  $O_2^+$  and  $CO_2^+$  recombination rate coefficients, and the ion-neutral rate coefficients. Further details of this calculation are provided in Table B1. Retaining the  $[e^-]^2$  and  $[e^-]^0$  terms in equation (B4), the absolute magnitudes of which are typically 1 to 2 orders of magnitude larger than the remaining two terms, yields a simple analytic expression for the electron density:

Quantities in square brackets are number densities, for example,  $[O]$  is the number density of neutral atomic oxygen.  $k_1$ ,  $k_2$ ,  $k_{10}$ ,  $\alpha_1$ , and  $\alpha_2$  are rate coefficients, the values of which are given in Table B1.  $\sigma_{CO_2}(\lambda)$  and  $\sigma_O(\lambda)$  are the wavelength-dependent ionization cross sections of  $CO_2$  and O, respectively.  $F(\lambda)$  is the ionizing flux.  $\eta_{CO_2}$  and  $\eta_O$  are the multiplicative factors accounting for electron-impact ionization of  $CO_2$  and O, respectively.

Production and loss of  $O_2^+$ :

$$[CO_2^+] [O] k_2 + [O^+] [CO_2] k_{10} = [O_2^+] [e^-] \alpha_1 \quad (B1)$$

Production and loss of  $O^+$ :

$$\eta_O [O] \sum_{\lambda=0.5 \text{ nm}}^{\lambda=\lambda_{\text{thresh}}} \sigma_O(\lambda) F(\lambda) + [CO_2^+] [O] k_1 = [O^+] [CO_2] k_{10} \quad (B2)$$

Production and loss of  $CO_2^+$ :

$$\eta_{CO_2} [CO_2] \sum_{\lambda=0.5 \text{ nm}}^{\lambda=\lambda_{\text{thresh}}} \sigma_{CO_2}(\lambda) F(\lambda) = [CO_2^+] [O] k_1 + [CO_2^+] [O] k_2 + [CO_2^+] [e^-] \alpha_2 \quad (B3)$$

**Table B1**  
*List of Photochemical Reactions*

Reaction	Rate coefficient ( $\text{cm}^3/\text{s}$ )
$CO_2^+ + O \rightarrow O^+ + CO_2$	$k_1 = 9.6 \times 10^{-11}$
$CO_2^+ + O \rightarrow O_2^+ + CO$	$k_2 = 1.6 \times 10^{-10}$
$O^+ + CO_2 \rightarrow O_2^+ + CO$	$k_{10} = 1.1 \times 10^{-9}$
$O_2^+ + e^- \rightarrow O + O$	$\alpha_1 = 2.4 \times 10^{-7} \left( \frac{300 \text{ K}}{T_e} \right)^{0.70}$
$CO_2^+ + e^- \rightarrow CO + O$	$\alpha_2 = 4.2 \times 10^{-7} \left( \frac{300 \text{ K}}{T_e} \right)^{0.75}$
Reaction	Rate ( $\text{cm}^{-3} \text{ s}^{-1}$ )
$CO_2 + h\nu \rightarrow CO_2^+ + e^-$	$[CO_2] \sum \sigma_{CO_2}(\lambda) F(\lambda)$
$O + h\nu \rightarrow O^+ + e^-$	$[O] \sum \sigma_O(\lambda) F(\lambda)$

Making the assumption that  $[O_2^+] = [e^-]$  (Knudsen et al., 1979; Taylor et al., 1979; Taylor et al., 1980) and solving this system of equations yields a cubic expression that can be solved for the electron density:

$$\begin{aligned} & [e^-]^3 \alpha_1 \alpha_2 + [e^-]^2 \alpha_1 [O] (k_1 + k_2) - [e^-] \alpha_2 [O] \sum_{\lambda=0.5 \text{ nm}}^{\lambda=\lambda_{\text{thresh}}} \sigma_O(\lambda) F(\lambda) \\ & - \left( [O] \sum_{\lambda=0.5 \text{ nm}}^{\lambda=\lambda_{\text{thresh}}} \sigma_O(\lambda) F(\lambda) + [CO_2] \sum_{\lambda=0.5 \text{ nm}}^{\lambda=\lambda_{\text{thresh}}} \sigma_{CO_2}(\lambda) F(\lambda) \right) [O] (k_1 + k_2) = 0 \end{aligned} \quad (B4)$$

## Acknowledgments

Venus Express radio occultation data can be obtained from the website ([http://www.radio-science.eu/?page\\_id=746&lang=en](http://www.radio-science.eu/?page_id=746&lang=en)). K. H. and P. W. acknowledge support from NASA Awards NNX16AJ54G and 80NSSC19K1533. Z. G. acknowledges support from NASA Award NNX12AN03H. The Venus Express Radio Science experiment VeRa is funded by the Deutsches Zentrum für Luft- und Raumfahrt (DLR) Bonn under Grant 50QM1004. We thank the personnel of the Venus Express project at ESTEC, ESOC, ESAC, JPL, and the ESTRACK ground station antennas for their continuous support. We thank two anonymous reviewers for their helpful comments.

## References

- Ambili, K. M., Babu, S. S., & Choudhary, R. K. (2019). On the relative roles of the neutral density and photo chemistry on the solar zenith angle variations in the V2 layer characteristics of the Venus ionosphere under different solar activity conditions. *Icarus*, 321, 661–670. <https://doi.org/10.1016/j.icarus.2018.12.001>
- Bauer, S. J., Brace, L. H., Hunten, D. M., Intriligator, D. S., Knudsen, W. C., Nagy, A. F., et al. (1977). 9. The Venus ionosphere and solar wind interaction. *Space Science Reviews*, 20(4), 413–430. <https://doi.org/10.1007/BF02186461>
- Brace, L. H., & Kliore, A. J. (1991). The structure of the Venus ionosphere. *Space Science Reviews*, 55(1-4), 81–163. <https://doi.org/10.1007/BF00177136>
- Brace, L. H., & Theis, R. F. (1984). Solar cycle effects upon the relationship of  $N_e$  and  $T_e$  in the F-region. *Advances in Space Research*, 4(1), 89–91. [https://doi.org/10.1016/0273-1177\(84\)90295-3](https://doi.org/10.1016/0273-1177(84)90295-3)
- Brace, L. H., & Theis, R. F. (1996). An extension of the VIRA electron temperature and density models to include solar cycle variations. *Advances in Space Research*, 17, 181–190. [https://doi.org/10.1016/0273-1177\(95\)00748-4](https://doi.org/10.1016/0273-1177(95)00748-4)
- Brace, L. H., Theis, R. F., Krehbiel, J. P., Nagy, A. F., Donahue, T. M., McElroy, M. B., & Pedersen, A. (1979). Electron temperatures and densities in the Venus ionosphere: Pioneer Venus Orbiter electron temperature probe results. *Science*, 203(4382), 763–765. <https://doi.org/10.1126/science.203.4382.763>
- Cravens, T. E., Gombosi, T. I., Kozyra, J., Nagy, A. F., Brace, L. H., & Knudsen, W. C. (1980). Model calculations of the dayside ionosphere of Venus—Energetics. *Journal of Geophysical Research*, 85, 7778–7786. <https://doi.org/10.1029/JA085iA13p07778>
- Cravens, T. E., Kliore, A. J., Kozyra, J. U., & Nagy, A. F. (1981). The ionospheric peak on the Venus dayside. *Journal of Geophysical Research*, 86, 11,323–11,329. <https://doi.org/10.1029/JA086iA13p11323>
- Elphic, R. C., Brace, L. H., Theis, R. F., & Russell, C. T. (1984). Venus dayside ionospheric conditions—Effects of ionospheric magnetic field and solar EUV flux. *Geophysical Research Letters*, 11, 124–127. <https://doi.org/10.1029/GL011i002p00124>
- Fallows, K., Withers, P., & Matta, M. (2015). Numerical simulations of the influence of solar zenith angle on properties of the M1 layer of the Mars ionosphere. *Journal of Geophysical Research: Space Physics*, 120, 6707–6721. <https://doi.org/10.1002/2014JA020947>
- Fox, J. L. (2004). Advances in the aeronomy of Venus and Mars. *Advances in Space Research*, 33, 132–139. <https://doi.org/10.1016/j.asr.2003.08.014>
- Fox, J. L., & Kliore, A. J. (1997). Ionosphere: Solar activity variations. In S. Bouger, S. Hunten, & R. Phillips (Eds.), *Venus II* (pp. 161–188). Tucson, AZ: The University of Arizona Press.
- Fox, J. L., & Sung, K. Y. (2001). Solar activity variations of the Venus thermosphere/ionosphere. *Journal of Geophysical Research*, 106, 21,305–21,336. <https://doi.org/10.1029/2001JA000069>
- Fox, J. L., & Yeager, K. E. (2009). MGS electron density profiles: Analysis of the peak magnitudes. *Icarus*, 200, 468–479. <https://doi.org/10.1016/j.icarus.2008.12.002>
- Gérard, J.-C., Bouger, S. W., López-Valverde, M. A., Pätzold, M., Drossart, P., & Piccioni, G. (2017). Aeronomy of the Venus upper atmosphere. *Space Science Reviews*, 212(3), 1617–1683. <https://doi.org/10.1007/s11214-017-0422-0>
- Girazian, Z. R. J. (2016). The Sun's influence on the vertical structure of the ionospheres of Venus and Mars (Ph.D. Thesis), Boston University.
- Girazian, Z., & Withers, P. (2013). The dependence of peak electron density in the ionosphere of Mars on solar irradiance. *Geophysical Research Letters*, 40, 1960–1964. <https://doi.org/10.1002/grl.50344>
- Girazian, Z., & Withers, P. (2015). An empirical model of the extreme ultraviolet solar spectrum as a function of  $F_{10.7}$ . *Journal of Geophysical Research: Space Physics*, 120, 6779–6794. <https://doi.org/10.1002/2015JA021436>
- Girazian, Z., Withers, P., Häusler, B., Pätzold, M., Tellmann, S., & Peter, K. (2015). Characterization of the lower layer in the dayside Venus ionosphere and comparisons with Mars. *Planetary and Space Science*, 117, 146–158. <https://doi.org/10.1016/j.pss.2015.06.007>
- Häusler, B., Pätzold, M., Tyler, G. L., Simpson, R. A., Bird, M. K., Dehant, V., et al. (2006). Radio science investigations by VeRa onboard the Venus Express spacecraft. *Planetary and Space Science*, 54, 1315–1335. <https://doi.org/10.1016/j.pss.2006.04.032>
- Hedin, A. E., Niemann, H. B., Kasprzak, W. T., & Seiff, A. (1983). Global empirical model of the Venus thermosphere. *Journal of Geophysical Research*, 88, 73–83. <https://doi.org/10.1029/JA088iA01p00073>
- Keating, G. M., & Bouger, S. (1987). Neutral upper atmospheres of Venus and Mars. *Advances in Space Research*, 7, 57–71. [https://doi.org/10.1016/0273-1177\(87\)90202-X](https://doi.org/10.1016/0273-1177(87)90202-X)
- Kim, J., Nagy, A. F., Cravens, T. E., & Kliore, A. J. (1989). Solar cycle variations of the electron densities near the ionospheric peak of Venus. *Journal of Geophysical Research*, 94, 11,997–12,002. <https://doi.org/10.1029/JA094iA09p11997>
- Kliore, A., Levy, G. S., Cain, D. L., Fjeldbo, G., & Rasool, S. I. (1967). Atmosphere and ionosphere of Venus from the Mariner V S-Band Radio Occultation Measurement. *Science*, 158, 1683–1688. <https://doi.org/10.1126/science.158.3809.1683>
- Kliore, A. J., & Luhmann, J. G. (1991). Solar cycle effects on the structure of the electron density profiles in the dayside ionosphere of Venus. *Journal of Geophysical Research*, 96, 21,281–21,289. <https://doi.org/10.1029/91JA01829>
- Kliore, A. J., & Mullen, L. F. (1989). The long-term behavior of the main peak of the dayside ionosphere of Venus during solar cycle 21 and its implications on the effect of the solar cycle upon the electron temperature in the main peak region. *Journal of Geophysical Research*, 94, 13,339–13,351. <https://doi.org/10.1029/JA094iA10p13339>
- Knudsen, W. C., Spennier, K., Whitten, R. C., Spreiter, J. R., Miller, K. L., & Novak, K. (1979). Thermal structure and major ion composition of the Venus ionosphere: First RPA results from Venus orbiter. *Science*, 203(4382), 757–758.
- Mariner Stanford Group (1967). Venus: Ionosphere and atmosphere as measured by dual-frequency radio occultation of Mariner V. *Science*, 158, 1678–1683. <https://doi.org/10.1126/science.158.3809.1678>

- Mendillo, M., Marusiak, A. G., Withers, P., Morgan, D., & Gurnett, D. (2013). A new semiempirical model of the peak electron density of the Martian ionosphere. *Geophysical Review Letters*, 40, 5361–5365. <https://doi.org/10.1002/2013GL057631>
- Nagy, A. F., Cravens, T. E., Smith, S. G., Taylor, H. A., & Brinton, H. C. (1980). Model calculations of the dayside ionosphere of Venus—Ionic composition. *Journal of Geophysical Research*, 85, 7795–7801. <https://doi.org/10.1029/JA085iA13p07795>
- Niemann, H. B., Hartle, R. E., Kasprzak, W. T., Spencer, N. W., Hunten, D. M., & Carignan, G. R. (1979). Venus upper atmosphere neutral composition: Preliminary results from the Pioneer Venus Orbiter. *Science*, 203(4382), 770–772. <https://doi.org/10.1126/science.203.4382.770>
- Niemann, H. B., Kasprzak, W. T., Hedin, A. E., Hunten, D. M., & Spencer, N. W. (1980). Mass spectrometric measurements of the neutral gas composition of the thermosphere and exosphere of Venus. *Journal of Geophysical Research*, 85, 7817–7827. <https://doi.org/10.1029/JA085iA13p07817>
- Pätzold, M., Häusler, B., Bird, M. K., Tellmann, S., Mattei, R., Asmar, S. W., et al. (2007). The structure of Venus' middle atmosphere and ionosphere. *Nature*, 450, 657–660. <https://doi.org/10.1038/nature06239>
- Pätzold, M., Tellmann, S., Häusler, B., Bird, M. K., Tyler, G. L., Christou, A. A., & Withers, P. (2009). A sporadic layer in the Venus lower ionosphere of meteoric origin. *Geophysical Research Letters*, 36, L05203. <https://doi.org/10.1029/2008GL035875>
- Peter, K., Pätzold, M., Molina-Cuberos, G., Witasse, O., González-Galindo, F., Withers, P., et al. (2014). The dayside ionospheres of Mars and Venus: Comparing a one-dimensional photochemical model with MaRS (Mars Express) and VeRa (Venus Express) observations. *Icarus*, 233, 66–82. <https://doi.org/10.1016/j.icarus.2014.01.028>
- Phillips, J. L., Luhmann, J. G., & Russell, C. T. (1985). Dependence of Venus ionopause altitude and ionospheric magnetic field on solar wind dynamic pressure. *Advances in Space Research*, 5, 173–176. [https://doi.org/10.1016/0273-1177\(85\)90286-8](https://doi.org/10.1016/0273-1177(85)90286-8)
- Rusch, D. W., & Cravens, T. E. (1979). A model of the neutral and ion nitrogen chemistry in the daytime thermosphere of Venus. *Geophysical Research Letters*, 6(10), 791–794. <https://doi.org/10.1029/GL006i010p00791>
- Schunk, R., & Nagy, A. (2009). *Ionospheres: Physics, plasma physics, and chemistry*. Cambridge, UK: Cambridge University Press.
- Taylor, Jr., Bauer, S. J., Daniell, R. E., Brinton, H. C., Mayr, H. G., & Hartle, R. E. (1981). Temporal and spatial variations observed in the ionospheric composition of Venus: Implications for empirical modelling. *Advances in Space Research*, 1(9), 37–51. [https://doi.org/10.1016/0273-1177\(81\)90217-9](https://doi.org/10.1016/0273-1177(81)90217-9)
- Taylor, H. A., Brinton, H. C., Bauer, S. J., Hartle, R. E., Cloutier, P. A., & Daniell, R. E. (1980). Global observations of the composition and dynamics of the ionosphere of Venus—Implications for the solar wind interaction. *Journal of Geophysical Research*, 85, 7765–7777. <https://doi.org/10.1029/JA085iA13p07765>
- Taylor, H. A. Jr., Brinton, H. C., Bauer, S. J., Hartle, R. E., Cloutier, P. A., Michel, F. C., et al. (1979). Ionosphere of Venus: First Observations of the Effects of Dynamics on the Dayside Ion Composition. *Science*, 203(4382), 755–757. <https://doi.org/10.1126/science.203.4382.755>
- Theis, R. F., Brace, L. H., Elphic, R. C., & Mayr, H. G. (1984). New empirical models of the electron temperature and density in the Venus ionosphere with application to transterminator flow. *Journal of Geophysical Research*, 89, 1477–1488. <https://doi.org/10.1029/JA089iA03p01477>
- Wedlund, C. S., Gronoff, G., Lilensten, J., Ménager, H., & Barthélémy, M. (2011). Comprehensive calculation of the energy per ion pair or W values for five major planetary upper atmospheres. *Annales Geophysicae*, 29, 187–195. <https://doi.org/10.5194/angeo-29-187-2011>